Local magnetism in MnSiPt rules the chemical bond

Helge Rosner[a,1], Andreas Leithe-Jasper[a], Wilder Carrillo-Cabrera[a], Walter Schnelle[a], Sarah V. Ackerbauer[a], Monika B. Gamza[a,b], and Yuri Grin[a,1]

[a]Max-Planck-Institut für Chemische Physik fester Stoffe, Chemische Metallkunde, 01187 Dresden, Germany; and [b]School of Physical Sciences and Computing, University of Central Lancashire, Preston, Lancashire, PR1 2HE, United Kingdom

Edited by Zachary Fisk, University of California, Irvine, CA, and approved June 6, 2018 (received for review April 24, 2018)

Among intermetallic compounds, ternary phases with the simple stoichiometric ratio 1:1:1 form one of the largest families. More than 15 structural patterns have been observed for several hundred compounds constituting this group. This, on first glance unexpected, finding is a consequence of the complex mechanism of chemical bonding in intermetallic structures, allowing for large diversity. Their formation process can be understood based on a hierarchy of energy scales: The main share is contributed by covalent and ionic interactions in accordance with the electronic needs of the participating elements. However, smaller additional atomic interactions may still tip the scales. Here, we demonstrate that the local spin polarization of paramagnetic manganese in the new compound MnSiPt rules the adopted TiNiSi-type crystal structure. Combining a thorough experimental characterization with a theoretical analysis of the energy landscape and the chemical bonding of MnSiPt, we show that the paramagnetism of the Mn atoms suppresses the formation of Mn–Mn bonds, deciding between competing crystal structures.

crystal structure | chemical bonding | local magnetism | TiNiSi structure type | intermetallic compounds

In solid state research, crystal–chemical concepts facilitate a fundamental understanding of crystal structures (1) and, combined with electronic counting rules (2), even enable the prediction for the composition and stability of structures and phases as well as their physical behavior (3). Basic bonding models—for example, the Zintl–Klemm concept—often describe crystal structures as being built of a covalent host substructure, which accommodates differently interacting guest atoms (4, 5). Chemical bonding (3, 6–8) within the host substructure dominates the structure's energy of formation. The most important energy contributions originate from the ionic and covalent interactions (9, 10). Since closely related structures show similar energies of formation, the host–guest interaction may become decisive for the finally realized structural pattern (3). Thus, besides the guest's total electron count, different ordering phenomena (11–13)—for example, site, charge, magnetic, or orbital order—and the specific orbital occupation might be crucial. However, direct experimental observations of those rather weak effects are often difficult, and their complex interplay merely becomes clear by applying a combination of precise analytical methods and theoretical calculations.

Here, we like to draw attention to another detail of the guest's electronic configuration, the "on-site" local magnetic polarization. This so-called paramagnetic local magnetic moment, which is seldom taken into account when considering chemical bonding in the solid state, is a prerequisite for an interatomic spin alignment that may or may not form at low enough temperatures. However, we demonstrate that the electronic configuration, even in the (disordered) paramagnetic state, can critically influence the topology of the crystal structure and rule the realization of a particular structural pattern.

Strong Curie-type paramagnetic behavior is caused by localized, partially filled orbitals exhibiting a large exchange splitting, which is a typical feature of $3d$ or $4f$ orbitals in transition-metal or rare-earth metal atoms, respectively (14). Whereas the $4f$ states are rarely chemically active, the $3d$ electrons of transition metals usually contribute significantly to the chemical bonding. Simultaneously, the respective $3d$ orbitals close to the Fermi level may carry large magnetic moments due to the strong local exchange splitting. MnSiX and MnGeX compounds (X = Ni, Co) are a perfect example. They crystallize in the structure-type TiNiSi, which can be described as a rather covalent network of X and Ge/Si species, leaving channels in between, where the Mn atoms with a large local magnetic moment (3 Bohr magnetons) are embedded (15).

Results and Discussion

The presence of potentially magnetic Co/Ni in the MnGe/SiX compounds is an obstacle for the investigation of the interplay between local magnetism and chemical bonding. To facilitate the interpretation, we synthesized the compound MnSiPt containing nonmagnetic Pt. MnSiPt is a paramagnet at high temperatures and reveals a complex magnetic ordering slightly above room temperature. To the best of our knowledge, there is no isostructural Mn-containing system that exhibits a nonmagnetic Mn site. The analyses of diffraction data on single crystals and powder showed that MnSiPt crystallizes in the orthorhombic TiNiSi structure type (Fig. 1 and *SI Appendix*). However, metallographic examination revealed a rather unexpected result: The MnSiPt grains in the microstructure show a specific stripe pattern (Fig. 2 and *SI Appendix*) caused by twinning. Usually, such effects are observed as a result of temperature-dependent structure transformations or of a mechanical deformation process.

Significance

A crystal structure can be understood as a result of bonding interactions (covalent, ionic, van der Waals, etc.) between the constituting atoms. If the forces caused by these interactions are equilibrated, the so-stabilized crystal structure should have the lowest energy. In such an atomic configuration, additional weaker atomic interactions may further reduce the total energy, influencing the final atomic arrangement. Indeed, in the intermetallic compound MnSiPt, a 3D framework is formed by polar covalent bonds between Mn, Si, and Pt atoms. Without taking into account the local spin polarization of manganese atoms, they would form Mn–Mn bonds within the framework. Surprisingly, the local magnetic moments of manganese prevent the formation of Mn–Mn bonds, thus changing decisively and significantly the final atomic arrangement.

Author contributions: H.R., A.L.-J., and Y.G. designed research; H.R., A.L.-J., W.C.-C., W.S., S.V.A., M.B.G., and Y.G. performed research; H.R., A.L.-J., W.C.-C., W.S., S.V.A., M.B.G., and Y.G. analyzed data; and H.R., A.L.-J., and Y.G. wrote the paper.

The authors declare no conflict of interest.

This article is a PNAS Direct Submission.

[1]To whom correspondence may be addressed. Email: rosner@cpfs.mpg.de or grin@cpfs.mpg.de.

This article contains supporting information online at www.pnas.org/lookup/suppl/doi:10.1073/pnas.1806842115/-/DCSupplemental.

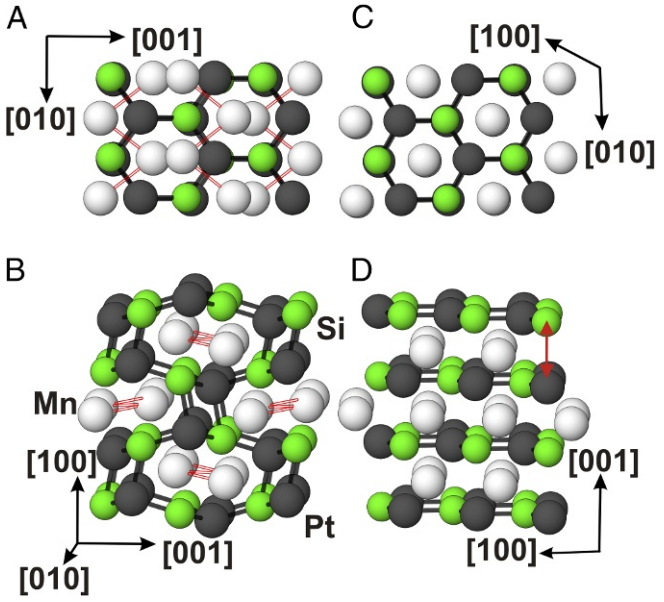

Fig. 1. Crystal structure of MnSiPt. (*A* and *B*) Observed crystal structure in the orthorhombic TiNiSi type: The shortest Pt–Si contacts (black bars) form layers of distorted hexagons, which are interconnected along the [100] direction, yielding eight-membered channels, where Mn–Mn zig-zag chains (red bars) are embedded. (*C* and *D*) In the hypothetical hexagonal ZrBeSi-type structure, the PtSi layers are composed of ideal hexagons, which are separated along the [001] direction. The orthorhombic structure can formally be derived from the hexagonal type by shortening Pt–Si contacts along [001] (red arrow) resulting in a buckling of the PtSi layers.

The structural similarity between the hexagonal and the orthorhombic phase, visible in Fig. 1, suggests that those two structural realizations may exhibit similar energies of formation, and the strong twinning indicates competing crystal formation mechanisms. Thus, the observed [011]-type twinning may originate from the hexagonal-to-orthorhombic phase transition (16–18).

Structural phase transitions, with the orthorhombic TiNiSi-type structure transforming during heating or by a change of composition to the geometrically related hexagonal ZrBeSi-type, were also found for ternary MnGeX compounds and MnSiNi (19–23). In TiGePt, the hexagonal structural pattern is an intermediate product of a TiNiSi-to-MgAgAs transformation (24).

Against expectations, the differential thermal analysis as well as high-temperature neutron powder diffraction on MnSiPt (see *SI Appendix*) did not detect any effects indicating a phase transition, apart from the melting point at 1,097 °C. Moreover, samples with a small deviation from the stoichiometric 1:1:1 composition and samples rapidly quenched from the melt via ultrafast splat cooling also did not evidence the expected hexagonal phase (see *SI Appendix*).

These unusual observations prompted us to estimate the stability of the TiNiSi- and ZrBeSi-type structural patterns for MnSiPt applying density-functional band structure calculations. Using the experimental crystallographic parameters, the calculated density of states indicated a strong hybridization between the low-lying Pt and Si states and a high contribution of Mn 3d electrons at the Fermi energy, consistent with the concept of energy scales presented above.

For non–spin-polarized calculations, however, an inspection of the calculated interatomic forces and the subsequent relaxation of the internal atomic positions (for the experimental lattice parameters) with respect to the total energy yields a large discrepancy between the optimized and the experimental atomic positions. This difference can be traced to the formation of

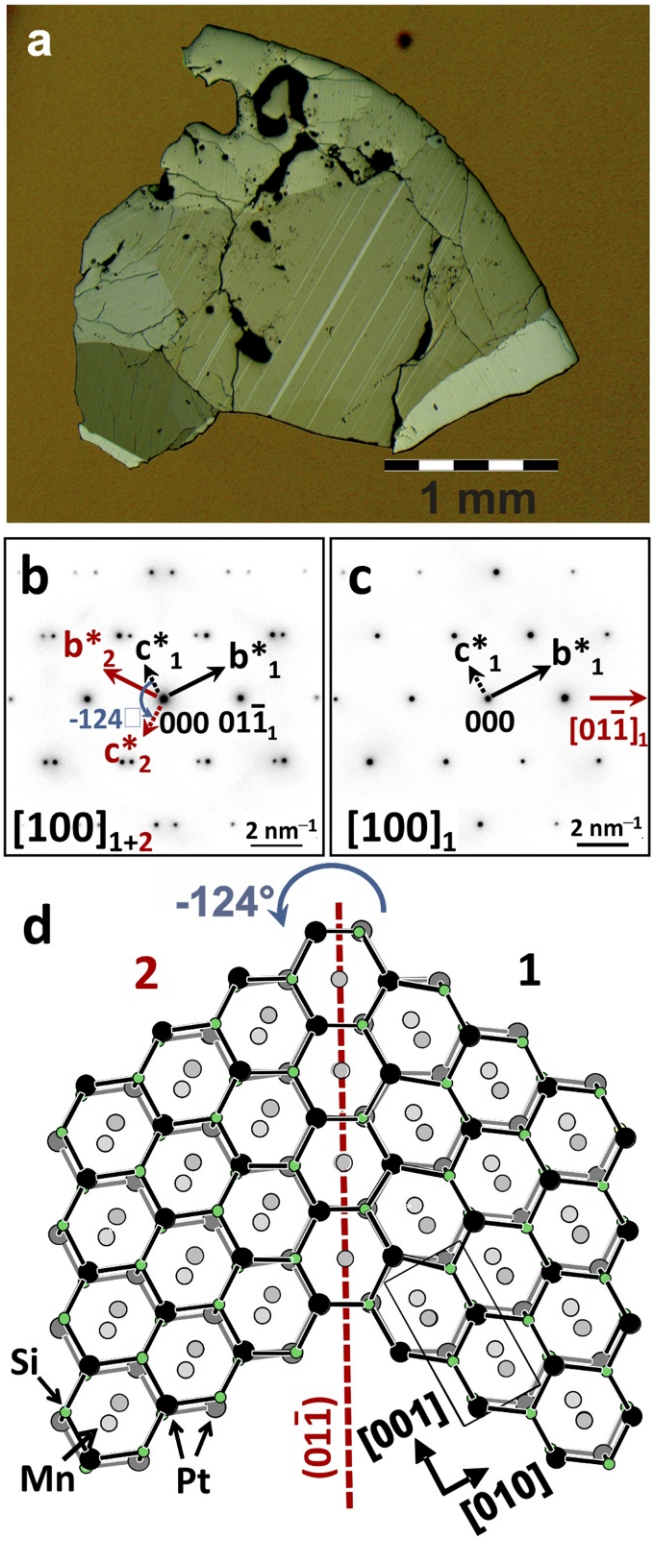

Fig. 2. Microstructure of MnSiPt. (*A*) Surface image of a polished cross-section in polarized light; differently orientated grains appear in different colors; parallel sharp stripes are so-called twins and occur in distinct orientations. (*B* and *C*) Electron diffraction patterns of a [011]-type twin and the twin interface region (twin + matrix) in MnSiPt viewed along [100]; the reciprocal unit cell axes are indicated; an anticlockwise rotation of 124.6° (around [100] axis) relates the two domains (twin + matrix). (*D*) Possible structural relation between the matrix (*C*) and [011]-type twins; common (01$\bar{1}$) plains (dashed lines) are layers of one sort of atoms only facilitating the connection between the twin and matrix.

Mn–Mn contacts, which are drastically (about 15%) too short compared with the experimental Mn–Mn distance. In sharp contrast, an almost perfect agreement (better than 1%) between experimental and calculated Mn–Mn distances was found when switching to spin-polarized calculations (the calculated positions and interatomic distances are provided in *SI Appendix*, Tables S6 and S7).

Most importantly, our calculations for several possible configurations of magnetically long-range ordered moments of Mn (for details, see *SI Appendix*) revealed that the influence of a specific magnetic order between the Mn sites (intersite exchange) is much smaller than the effect caused by the local magnetic moment of each Mn atom in the paramagnetic state. According to these results, the formation of a local Mn moment is responsible for more than 90% of the energy gain compared with a non–spin-polarized state. This large energy gain has been confirmed by another type of calculation applying the coherent potential approximation (CPA) (25) in the disordered local moment (DLM) approach (see *SI Appendix*). This approach, modeling a random distribution of Mn atoms with spin up or down, yields the formation of large local moments of about 3 Bohr magnetons at the Mn sites, irrespective of a long-range magnetic order. Moreover, the computed magnetic moment is in very good agreement with the saturation moment measured at low temperatures (2 K) in a high magnetic field of 60 T (see *Inset* in Fig. 3).

Finally, the energy versus formula-unit volume dependence for the structure types TiNiSi and ZrBeSi with and without local Mn magnetism sharpens the picture of the paramagnetism of Mn as a crucial ingredient for the formation of the crystal structure of MnSiPt. Both structure types exhibit a large energy gain due to local Mn magnetism (see Fig. 3). Unexpectedly, we find that for the nonmagnetic situation, the ZrBeSi structure type is significantly more stable (lower in energy). However, the stabilization of the TiNiSi structure type by the local Mn moment (about 630 meV per formula unit) is considerably larger than in the ZrBeSi type (about 400 meV per formula unit), finally making the TiNiSi type more stable. These results are robust with respect to computational details, especially the choice of the density functional (DFT) [LDA or general gradient approximation (GGA); cf. *SI Appendix*]. Interestingly, the energy difference between the TiNiSi structure type and the ZrBeSi structure type (about 230 meV) is of the same order as the formation temperature (melting point about 1370 K; see *SI Appendix*, Fig. S5). This might suggest that the origin of the observed twinning is related to a close competition of both phases at elevated temperatures.

To understand the chemical background of the stabilization of the TiNiSi structure for the MnSiPt compound, an analysis of atomic interactions in real space (i.e., in the language of chemistry) was performed using the Electron Localizability Indicator in its ELI-D representation (26–28). This bonding indicator describes the behavior of electron pairs in real space and was shown to be an efficient tool for the detection and visualization of chemical bonds. In particular, it is useful for the study of two- and multicenter bonds, as well as lone pairs as elements contributing to the chemical bonding in intermetallic compounds.

For MnSiPt, ELI-D was calculated for two models, one with the experimental structural parameters and another one with the optimized lattice parameters and atomic coordinates. As before, the calculations were performed with and without taking into account spin polarization (Fig. 4). In all cases, the distribution of ELI-D in the (010) plane reveals local maxima on the lines connecting Pt and Si or Mn and Si atoms, thus visualizing the according covalent interactions within the framework. When the spin polarization is not accounted for, an ELI-D maximum is obtained between the Mn atoms in the (200) and (100) planes, indicating the Mn–Mn bond. This bonding feature becomes more pronounced after optimization of the structural parameters. Once the spin polarization is taken into account, the ELI-D maximum in this region of the structure disappears. Consequently, the Mn atoms shift away from each other during the optimization procedure. The ELI-D thus drastically illustrates the suppression of covalent Mn–Mn bonding due to the local Mn spin polarization.

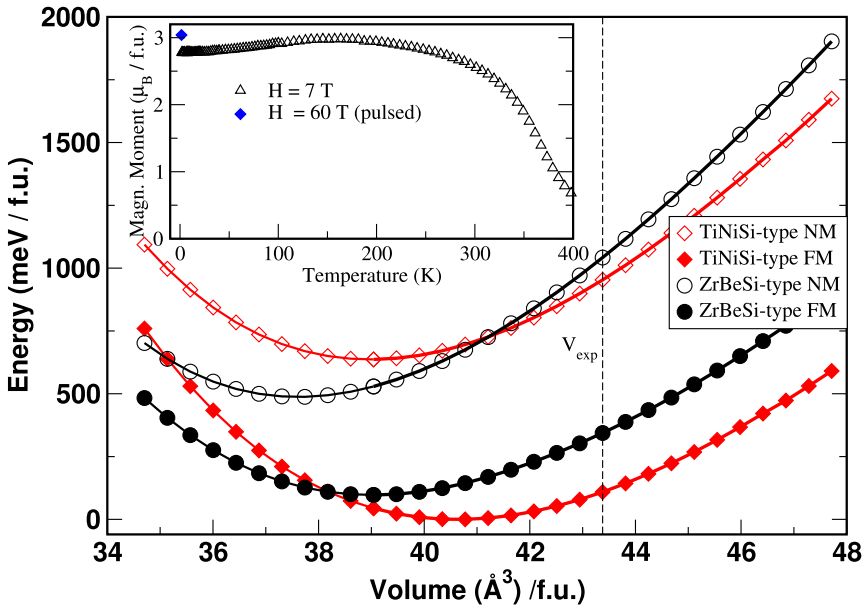

Fig. 3. Calculated formation energy versus formula-unit volume of MnSiPt for the experimentally observed TiNiSi-type (diamonds) and the hypothetical ZrBeSi-type structures (circles). Whereas for a nonmagnetic calculation (open symbols) the ZrBeSi type is more favorable in energy, spin-polarized calculations (filled symbols) favor the TiNiSi type. The calculated equilibrium volume is about 5% smaller than the experimental value (vertical dashed line indicates experimentally observed volume), as expected for local density approximation (LDA) calculations. *Inset* shows the temperature-dependent magnetization measured in a magnetic field of 7 T (open triangles) and the saturation magnetization of about 3 μ_B at 2 K in a pulsed field of 60 T (filled diamonds).

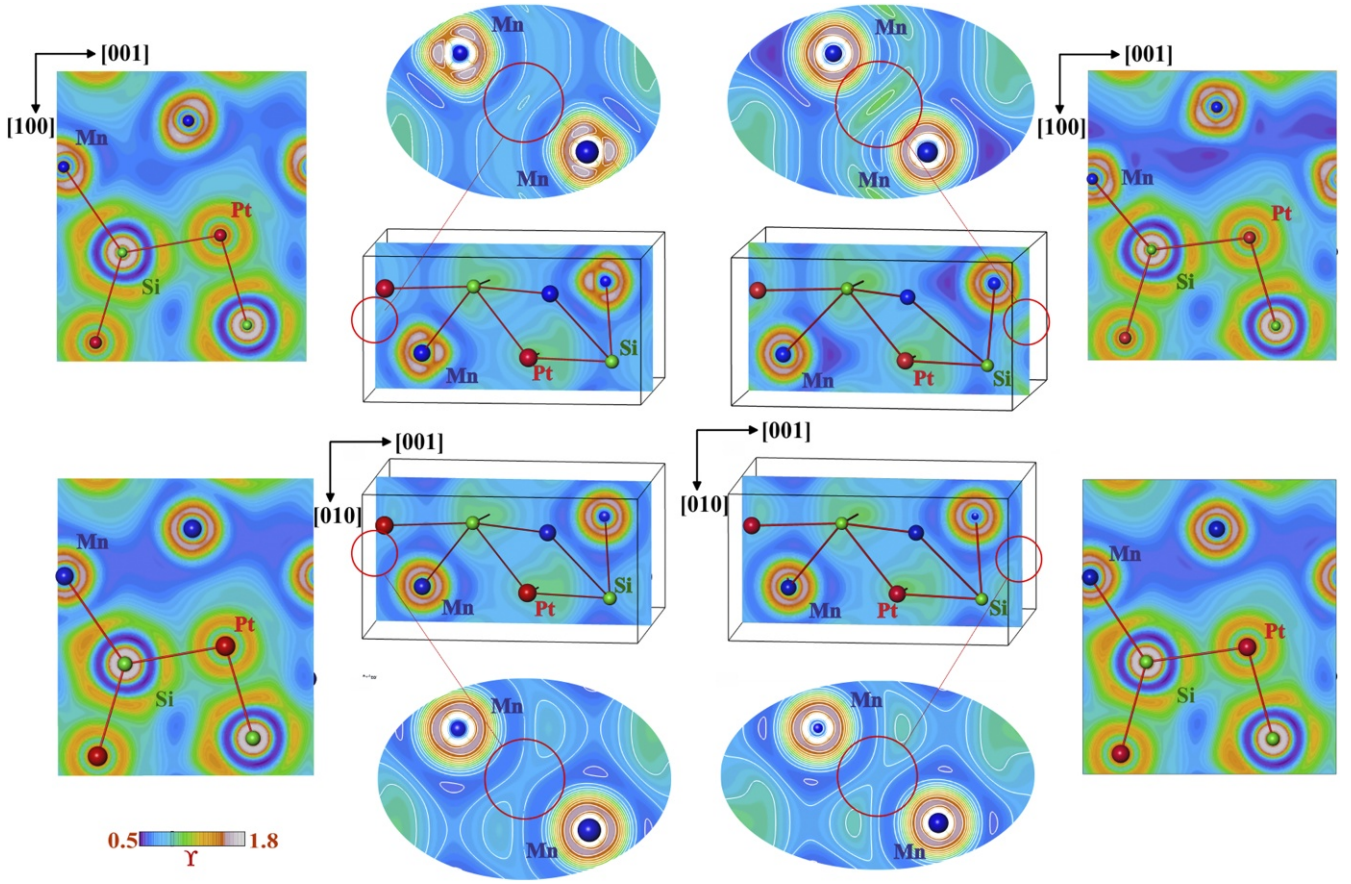

Fig. 4. Electron localizability indicator (ELI-D) in MnSiPt: Non–spin-polarized (upper row) and spin-polarized calculation (bottom row) for experimental (left side) and optimized (right side) structural parameters. The distribution of ELI-D in the characteristic planes (010) and (200) is shown. Local maxima on the Mn–Si and Pt–Si contacts in the (010) planes visualize the according covalent interactions. Red circles show the regions of the Mn–Mn interactions: In the non–spin-polarized case, local maxima indicating Mn–Mn bond formation are visible and are particularly strong for the optimized structure. The spin-polarized calculations show no local maxima in this region.

Conclusion and Summary

In conclusion, we find that the local magnetic polarization of the Mn atoms in MnSiPt has two crucial consequences:

i) The structure forms in the TiNiSi type rather than in the ZrBeSi type.
ii) The formation of direct Mn–Mn bonds is suppressed, since the energy gain due to bond formation is significantly smaller than the on-site magnetic interactions.

Therefore, after formation of the covalent bonds between Pt and Si as well as between Mn and Si, the strong Mn intraatomic exchange is the key factor for the stability of the crystal structure. In competition against the Mn–Mn bond formation, intraatomic magnetic interactions determine the topology of the local atomic arrangement in the TiNiSi-type crystal structure in MnSiPt.

Materials and Methods

Synthesis. Mixtures of the elements (Mn granules, Alfa Aesar, 99.9998%; Pt granules, ChemPur, 99.95%; Si granules, Alfa Aesar, 99.9999%) with the nominal composition MnSiPt were arc melted in purified argon atmosphere. The as-cast samples were put into glassy carbon crucibles, which were then enclosed in tantalum ampoules under argon atmosphere. To protect the tantalum from corrosion at high temperatures, the containers were sealed in evacuated quartz ampoules. The samples were annealed at 900°C for 1 wk, respectively, and finally quenched in water.

X-Ray Diffraction. Single-crystal X-ray diffraction intensity measurements of MnSiPt were performed using a Rigaku AFC-7 diffractometer (Mo Kα radiation, λ = 0.71073 Å) equipped with a Mercury CCD. The crystal structures were determined by direct methods using the WinCSD program (29). For powder XRD, see *SI Appendix*.

Metallography. For the metallographic cross-sections, the sample pieces were embedded in conductive resin, subsequently grinded, and polished. Microstructures of the samples were analyzed using optical and electron microscopy.

Transmission Electron Microscopy. For the transmission electron microscopy (TEM) study, oriented cross-sections of twin interfaces were extracted from a metallographic polished specimen using the focused ion beam (FIB) lift-out technique in a Quanta 200 3D dual beam FIB/SEM microscope (FEI, Eindhoven) equipped with an Omniprobe micromanipulator.

Magnetic Measurements. Magnetization measurements on a polycrystalline sample were carried out in the temperature range of 1.8 K to 400 K, applying magnetic fields up to 7 T in a SQUID magnetometer MPMS-XL7 (Quantum Design).

High-Field Measurements. Pulsed-field magnetization measurements in fields up to 60 T were performed at T = 1.4 K in the Dresden High Magnetic Field Laboratory. Details of the measurement procedure are described in ref. 30.

Computational Procedures.

i) FPLO (Full-potential local-orbital minimum-basis code): Relativistic DFT electronic structure calculations were performed using the full-potential FPLO code (31), version fplo9.09-43. For the exchange-correlation

potentials, the parametrizations of Perdew–Wang (LDA) (32) and of Perdew–Burke–Ernzerhof (GGA) (33) were chosen. To obtain precise band structure and Fermi surface information, the calculations were carried out on a well-converged mesh of 4,320 *k*-points (15 $\times$24$\times$ 12 mesh, 728 points in the irreducible wedge of the Brillouin zone).

ii) ELI: Chemical bonding analysis was performed in position space by using the ELI-D (26–28, 34), which was calculated on a 0.05 Bohr-radii mesh by a module implemented into the package (35). The topological analysis of the scalar field was performed with the program DGrid (36).

ACKNOWLEDGMENTS. For experimental support, we acknowledge Ulrich Burkhardt (metallography), Horst Borrmann (X-ray diffraction measurements), and Marcus Schmidt (differential thermal analysis). We thank Ulrike Nitzsche for technical assistance and Anatoly Senyshyn for fruitful discussions. We also thank the Dresden High Magnetic Field Laboratory for support with the high magnetic field measurements.

1. Pearson WB (1972) *The Crystal Chemistry and Physics of Metals and Alloys*, Wiley Series on the Science and Technology of Materials (Wiley-Interscience, New York).
2. Pauling L (2010) *The Nature of the Chemical Bond and the Structure of Molecules and Crystals: An Introduction to Modern Structural Chemistry* (Cornell Univ Press, Ithaca, NY), 3rd Ed.
3. Pettifor D (1996) Phenomenology and theory in structural prediction. *J Phase Equilib* 17:384–385.
4. Nesper R (1991) Bonding patterns in intermetallic compounds. *Angew Chem Int Ed Engl* 30:789–795.
5. Grin Y (2013) *Comprehensive Inorganic Chemistry II*, eds Reedijk J, Poeppelmeier KR (Elsevier, Amsterdam), Vol 2, 2nd Ed, pp 359–374.
6. Skriver H (1985) Crystal-structure from one-electron theory. *Phys Rev B* 31:1909–1923.
7. Pettifor DG (1996) *Bonding and Structure of Molecules and Solids*, Oxford Science Publications (Clarendon Press, Oxford).
8. Pettifor D (1985) Phenomenological and microscopic theories of structural stability. *J Less Common Met*. 114:7–15.
9. Bende D, Wagner FR, Sichevych O, Grin Y (2017) Chemical bonding analysis as a guide for the preparation of new compounds: The case of VIrGe and HfPtGe. *Angew Chem Int Ed* 56:1313–1318.
10. Wagner FR, Bende D, Grin Y (2016) Heteropolar bonding and a position-space representation of the (8-N) rule. *Dalton Trans* 45:3236–3243.
11. Miller GJ (1998) The "coloring problem" in solids: How it affects structure, composition and properties. *Eur J Inorg Chem* 1998:523–536.
12. Pöttgen R (2014) Coloring, distortions, and puckering in selected intermetallic structures from the perspective of group-subgroup relations. *Z Anorg Allg Chem* 640:869–891.
13. Hotta T (2006) Orbital ordering phenomena in d- and f-electron systems. *Rep Prog Phys* 69:2061–2155.
14. Coey JMD (2009) *Magnetism and Magnetic Materials*. (Cambridge Univ Press, Cambridge, UK).
15. Landrum GA, Hoffmann R, Evers J, Boysen H (1998) The TiNiSi family of compounds: Structure and bonding. *Inorg Chem* 37:5754–5763.
16. Torrens-Serra J, et al. (2014) The effect of annealing on the transformation, and the microstructure of $Mn_{(1-x)}Cr_xCoGe$ alloys. *Mater Charact* 93:24–31.
17. Audebrand N, Ellner M, Mittemeijer EJ (2003) The displacive phase transformation $Co_2Ge(h) \rightarrow Co_2Ge(1)$. *J Alloys Compounds* 353:228–232.
18. Jin Y, Chaturvedi MC (1996) Crystallographic study of Ni_2Ge phase in binary Ni-Ge alloy system. *Acta Mater* 44:3833–3845.
19. Jeitschko W (1975) High-temperature X-ray study of displacive phase-transition in MnCoGe. *Acta Crystallogr Sect B Struct Crystallogr Cryst Chem* 31:1187–1190.
20. Johnson V (1975) Diffusionless orthorhombic to hexagonal transitions in ternary silicides and germanides. *Inorg Chem* 14:1117–1120.
21. Fjellvag H, Andresen AF (1985) On the crystal-structure and magnetic-properties of MnNiGe. *J Magn Magn Mater* 50:291–297.
22. Kaprzyk S, Niziol S (1990) The electronic-structure of CoMnGe with the hexagonal and orthorhombic crystal-structure. *J Magn Magn Mater*. 87:267–275.
23. Bazela W, Szytula A, Todorovic J, Zieba A (1981) Crystal and magnetic-structure of the $NiMnGe_{1-n}Si_n$ system. *Phys Status Solidi A* 64:367–378.
24. Ackerbauer SV, et al. (2012) Structural transformation with "negative volume expansion": Chemical bonding and physical behavior of TiGePt. *Chem Eur J* 18:6272–6283.
25. Koepernik K, Velicky B, Hayn R, Eschrig H (1998) Analytic properties and accuracy of the generalized Blackman-Esterling-Berk coherent-potential approximation. *Phys Rev B* 58:6944–6962.
26. Kohout M (2004) A measure of electron localizability. *Int J Quan Chem* 97:651–658.
27. Kohout M (2007) Bonding indicators from electron pair density functionals. *Faraday Discuss* 135:43–54.
28. Wagner FR, Bezugly V, Kohout M, Grin Y (2007) Charge decomposition analysis of the electron localizability indicator: A bridge between the orbital and direct space representation of the chemical bond. *Chem Eur J*. 13:5724–5741.
29. Akselrud L, Grin Y (2014) WinCSD: Software package for crystallographic calculations (version 4). *J Appl Crystallogr* 47:803–805.
30. Tsirlin AA, et al. (2009) Exploring the spin-1/2 frustrated square lattice model with high-field magnetization studies. *Phys Rev B* 80:132407.
31. Koepernik K, Eschrig H (1999) Full-potential nonorthogonal local-orbital minimum-basis band-structure scheme. *Phys Rev B* 59:1743–1757.
32. Perdew JP, Wang Y (1992) Accurate and simple analytic representation of the electron-gas correlation energy. *Phys Rev B* 45:13244–13249.
33. Perdew J, Burke K, Ernzerhof M (1996) Generalized gradient approximation made simple. *Phys Rev Lett* 77:3865–3868.
34. Pendas AM, Kohout M, Blanco MA, Francisco E (2012) *Modern Charge Density Analysis*, eds Gatti C, Macchi P (Springer, Dordrecht, The Netherlands), pp 303–358.
35. Ormeci A, Rosner H, Wagner F, Kohout M, Grin Y (2006) Electron localization function in full-potential representation for crystalline materials. *J Phys Chem A*. 110:1100–1105.
36. DGrid (2011) Version 4.6. www2.cpfs.mpg.de/∼kohout/Documents/DGrid-4.6.pdf. Accessed June 29, 2018.